Koiter–Newton Based Model Reduction for Large Deflection Analysis of Wing Structures

Sinha, Kautuk; Alijani, Farbod; Krüger, Wolf R.; Breuker, Roeland De

DOI
10.2514/1.J062514

Publication date
2023

Document Version
Final published version

Published in
AIAA Journal

Citation (APA)
Sinha, K., Alijani, F., Krüger, W. R., & Breuker, R. D. (2023). Koiter–Newton Based Model Reduction for Large Deflection Analysis of Wing Structures. *AIAA Journal*, *61*(8), 3608-3617. https://doi.org/10.2514/1.J062514

AIAA JOURNAL
Vol. 61, No. 8, August 2023

Koiter–Newton Based Model Reduction for Large Deflection Analysis of Wing Structures

Kautuk Sinha*
DLR, German Aerospace Center, 37073 Goettingen, Germany
Farbod Alijani†
Delft University of Technology, 2628 CN Delft, The Netherlands
Wolf R. Krüger‡
DLR, German Aerospace Center, 37073 Goettingen, Germany
and
Roeland De Breuker§
Delft University of Technology, 2629 HS Delft, The Netherlands

https://doi.org/10.2514/1.J062514

Wing structures subjected to large deflections are prone to nonlinear load-deflection behavior. Geometric nonlinearities can arise due to the accompanying large rotations and in-plane deflections that manifest in the form of stiffening effects in the nonlinear static response. To account for these nonlinearities, reduced-order modeling techniques in combination with nonlinear finite element formulations have been previously proposed. However, these methods often have a limited range of validity due to linear eigenmode-based formulations with assumptions of small rotations. In this paper, a large deflection analysis framework based on the Koiter–Newton model reduction technique is presented. It is demonstrated that the reduced model in its basic form is ineffective for large deflection analysis. To resolve this, an incremental updating procedure is used for the reduced-order model that incorporates the necessary nonlinear effects. The model updating enables the computation of nonlinear response for a large range of deflections.

I. Introduction

CANTILEVERED structures can be prominently found in a wide variety of engineering applications ranging from aircraft wings to micromechanical resonators. In these applications, the loading conditions are such that the structure exhibits nonlinear behavior while undergoing large rotations and large deformations. In general, nonlinearities are manifested in the form of geometric stiffening due to large rotations, large strains due to large deformations, and follower forces, i.e., change in direction of the force along with the deflecting geometry. The geometric stiffening effect is especially influential in flexible structures that have a low bending stiffness due to the pronounced coupling between the out-of-plane displacement and in-plane stretching. Additionally, the large rotation of the structure causes an apparent reduction in the moment arm [1], which results in a varying moment distribution across the load trajectory.

The advent of high-aspect-ratio (HAR) and flexible-wing aircraft designs, such as the high-altitude long-range and endurance aircraft [2], has driven the increased interest in nonlinear modeling of wing structures. The primary advantage of such wing designs is the gain in the aerodynamic efficiency achieved due to the induced drag reduction. However, a major drawback is that the traditional linear analyses techniques become redundant due to the inherent nonlinearities.

A considerable amount of progress has been achieved in the last decades in the analyses and prediction of geometrically nonlinear effects. A majority of the methods developed in the past have explored the geometrically exact beam (GEB) formulations in analyzing the flexible wings [3–6]. Equivalent one-dimensional (1-D) nonlinear beam model formulations have been used for studying flexible flying wings in Refs. [7,8]. In Ref. [9], the dynamics of a flexible wing was modeled using a geometrically exact composite beam description. A formulation for curved and twisted anisotropic beams based on the intrinsic geometrically exact theory was presented in Ref. [10]. This has been subsequently applied in studying the flight dynamics of a highly flexible flying wing configuration [11]. A nonlinear aeroelastic model based on a GEB formulation has been developed in Ref. [12] for large wind turbine blades. The main idea in these methods was the derivation of equivalent beam properties that replicate the global structural response of the wing structure with no assumptions with respect to beam kinematics. A strain-based geometrically nonlinear beam model was used in Ref. [13], where extensional strain, bending, and torsional curvatures were defined as independent degrees of freedom; and the governing equations of the beam and the strain-displacement kinematics were solved iteratively. In this work, the authors describe this method as being efficient for the static case because the stiffness matrix remains constant; however, the method loses this advantage for transient problems because the damping and inertia need to be updated. In Ref. [14], a model reduction method based on eigenmode decomposition of the Jacobian matrix of the system has been used in combination with a GEB model for studying the dynamic gust response of a realistic aircraft. A limitation of using equivalent beam formulations is that it can lead to oversimplification of complex geometries, which eliminates the local effects involving the interactions of structural subcomponents.

Alternately, some researchers have deviated from the beam formulations in an attempt to achieve generality for complex structures. A finite element (FE) compatible approach based on the equivalent linearization method for large deflection analysis has been presented in Ref. [15]. The method has been shown to be accurate for the class of problems dealing with a high degree of bending–stretching coupling. However, it has been highlighted that for cantilevered structures, which have significant in-plane motion, the existing nonlinear formulation is inapplicable due to the utilization of linear

Received 5 October 2022; revision received 6 March 2023; accepted for publication 6 March 2023; published online 10 April 2023.

*Researcher, Loads Analysis and Aeroelastic Design, Institute of Aeroelasticity; kautuk.sinha@dlr.de.
†Associate Professor, Faculty of Mechanical, Maritime and Materials Engineering.
‡Head of Department, Loads Analysis and Aeroelastic Design, Institute of Aeroelasticity.
§Associate Professor, Faculty of Aerospace Engineering.

eigenmodes in the reduction basis. A nonlinear reduced-order modeling technique for a wing structure was presented in Ref. [16]. The reduction basis matrix was based on the concept of dual modes [17] that were derived from nonlinear displacement fields obtained from a set of nonlinear static analyses. The dual modes were appended to linear modes in the basis matrix to capture the membrane stretching effect. An extended modal approach was presented in Ref. [18–20] that was directly applicable to generic FE models. The method used a strain energy-based formulation in which higher-order stiffness terms were computed as derivatives of the total strain energy of the system. The nonlinear displacement field was constructed as a function of generalized displacements with the utilization of higher-order mode components. However, the method was shown to be accurate up to moderately large deflections (25% of the semispan).

In a novel mode-based approach called the modal rotation method (MRM) [21], curvature modes are used to obtain a reduced model. The underlying premise is that the curvatures, unlike displacements, can always be linearized through sufficient discretization; therefore, a linear superposition of curvature modes is a valid assumption. The nonlinear stiffness is not explicitly computed; instead, the nonlinear terms are incorporated as iterative corrections to the generalized forces. The simulation times using this approach have been shown to be significantly fast even for complex three-dimensional (3-D) structures undergoing highly nonlinear deformations. In Ref. [22], a two-step reduction technique was presented, which was subsequently applied to study the nonlinear aeroelastic characteristics of a transport aircraft [23]. This involved a static condensation of the 3-D structure to obtain a 1-D subdomain. Further reduction was obtained by using the mode-based Galerkin projection of the intrinsic nonlinear equations. The approach has been shown to be accurate for moderately large deflections (up to 20% span) with attached flows.

This paper presents the first application of the Koiter–Newton model reduction technique [24–26] to the large deflection analyses of cantilevered structures. A compatible FE framework is developed with the objective of applying the method to any generic structure. The nonlinearity in the system is modeled using higher-order stiffness tensors, whereas the kinematics of the system is described using the nonlinear Green–Lagrange equations. It is shown that the Koiter–Newton reduction in its basic form is ineffective in large deflection analyses of cantilevered structures. To circumvent this issue, the concept of convective element coordinates [27] is used, which accounts for the large rotation of the structure through incremental model updating and iterative force correction. A nonlinear predictor, obtained from solving the reduced model, enables larger load increments to be applied in comparison to linear formulations. The approach has been verified through nonlinear benchmark problems. Additionally, the method is validated through comparisons with experimental data obtained from a highly flexible wind-tunnel test model called the Pazy wing [28]. Finally, the framework is applied to a wing box model and compared to the results from MSC Nastran to demonstrate its applicability to generic 3-D structures.

II. Theoretical Formulation

In the present formulation, the effect of geometric nonlinearities is considered and the material is assumed to be linear elastic; whereas the boundary conditions remain unchanged throughout the analysis. The following subsections give a summary of the formulation implemented in the framework.

A. Governing Equations

The internal force of the structure, which is a function of the displacement vector $\boldsymbol{u}$, can be expanded about the equilibrium position using the Taylor series expansion, as described in the Eq. (1), for a statically loaded system:

$$\boldsymbol{L}(\boldsymbol{u}) + \boldsymbol{Q}(\boldsymbol{u},\boldsymbol{u}) + \boldsymbol{C}(\boldsymbol{u},\boldsymbol{u},\boldsymbol{u}) + O(\|\boldsymbol{u}^4\|) = \boldsymbol{f}_{\text{ext}} \tag{1}$$

Here, $\boldsymbol{L}$ describes a linear function corresponding to the tangent stiffness matrix; $\boldsymbol{Q}$ and $\boldsymbol{C}$ describe the quadratic and cubic functions corresponding to the third-order and fourth-order stiffness tensors, respectively; $O(||\boldsymbol{u}^4||)$ implies higher-order terms; $\boldsymbol{f}_{\text{ext}}$ describes a vector of external loads; and $\boldsymbol{u}$ is a vector of displacements and rotations.

The stiffness tensors of the full FE model are computed using strain energy-based FE formulations. Presently, two types of elements are used: planar beam element with three degrees of freedom (DOFs) per node, for which the formulation and shape functions were discussed in Refs. [25,29], and a high performance three-node triangle flat shell element with six DOFs per node, which was discussed in detail in Refs. [25,26,30–32]. It is notable that the choice of finite elements does not have an influence on the generality of the process. However, for simplicity in the further discussions presented here, the planar beam element will be referred to.

Consistent with the large deflection and finite strain assumption, the Green–Lagrange strain model is used to describe the strain-displacement relationship. For beam elements, the axial strain ϵ and the curvature χ are given by

$$\epsilon = u_{,x} + \frac{1}{2}(u_{,x}^2 + w_{,x}^2) \tag{2}$$

$$\chi = w_{,xx} \tag{3}$$

where u and w are nodal displacements in the x and y directions, and the subscript, x indicates the derivative with respect to the x direction. Because the nonlinearity lies in the axial component of the strain description, only the axial strain energy is initially considered.

The axial strain energy U for the Euler–Bernoulli beam is given by

$$U = \frac{1}{2}\int_0^L EA\epsilon^2 \,\mathrm{d}s \tag{4}$$

where E is the elastic modulus, A is the area of the cross section, s is the length of a differential element of the beam, and L is the total length of the beam. When discretized in an FE framework, the strain energy U_{elem} of each beam element of length l_{elem} can be obtained using

$$U_{\text{elem}} = \frac{1}{2}Al_{\text{elem}}\epsilon' E\epsilon \tag{5}$$

It is notable that in Eq. (5), a constant strain is enforced by averaging the strain over the length of the element. This is done to avoid the locking phenomena in FE formulations, as discussed in Ref. [29]. The internal force vector corresponding to axial forces can then be derived as the first derivative of the strain energy:

$$f_i = EAl_{\text{elem}}\epsilon\frac{\partial\epsilon}{\partial q_i} \tag{6}$$

where $\boldsymbol{q} = [\boldsymbol{u} \quad \boldsymbol{v} \quad \boldsymbol{\theta}]$ consists of the element degrees of freedom.

Similarly, the stiffness tensors can be computed as higher-order derivatives of the strain energy. Because the strain energy expression comprises up to fourth-order terms in displacement derivatives, the computation of stiffness tensors is limited to the cubic stiffness term. If N is the total number of degrees of freedom in the model and i, j, k, and l range from one to N, then the elements of these stiffness tensors are

$$L_{ij} = EAl_{\text{elem}}\left(\epsilon\frac{\partial^2\epsilon}{\partial q_i\partial q_j} + \frac{\partial\epsilon}{\partial q_i}\frac{\partial\epsilon}{\partial q_j}\right) \tag{7}$$

$$Q_{ijk} = \frac{EAl_{\text{elem}}}{2}\left(\frac{\partial\epsilon}{\partial q_j}\frac{\partial^2\epsilon}{\partial q_i\partial q_k} + \frac{\partial\epsilon}{\partial q_i}\frac{\partial^2\epsilon}{\partial q_j\partial q_k} + \frac{\partial\epsilon}{\partial q_k}\frac{\partial^2\epsilon}{\partial q_i\partial q_j}\right) \tag{8}$$

$$C_{ijkl} = \frac{EAl_{\text{elem}}}{6}\left(\frac{\partial^2\epsilon}{\partial q_i\partial q_l}\frac{\partial^2\epsilon}{\partial q_j\partial q_k} + \frac{\partial^2\epsilon}{\partial q_j\partial q_l}\frac{\partial^2\epsilon}{\partial q_i\partial q_k} + \frac{\partial^2\epsilon}{\partial q_k\partial q_l}\frac{\partial^2\epsilon}{\partial q_i\partial q_j}\right) \tag{9}$$

It is recalled that these expressions are computed using the axial strain component. To obtain the complete set of stiffness tensors required for the finite element equations, a bending stiffness component $\boldsymbol{K_b}$ must be added to the stiffness matrix $\boldsymbol{L}$. This bending stiffness term $\boldsymbol{K_b}$ is obtainable from the curvature [32] and is defined in Appendix A. Furthermore, the basic FE expressions relevant to the flat shell elements are defined in Appendix B. For a comprehensive discussion on the flat shell elements used in this work, the reader is referred to Refs. [26,32].

B. Koiter–Newton Model Reduction

As seen in Sec. II.A, the governing equation comprises a nonlinear system of equations that is normally solved iteratively through predictor–corrector methods. However, for complex models comprising a large number of degrees of freedom, it is often computationally expensive to obtain a solution of such a system; moreover, it can lead to convergence issues. Model order reduction is a technique used to alleviate the computational costs by reducing the system size while maintaining the accuracy in the solution. This section summarizes the steps in the Koiter–Newton reduction technique [24–26]. For this, we write Eq. (1) as follows:

$$\boldsymbol{L}(\boldsymbol{u}) + \boldsymbol{Q}(\boldsymbol{u},\boldsymbol{u}) + \boldsymbol{C}(\boldsymbol{u},\boldsymbol{u},\boldsymbol{u}) = \boldsymbol{F}\phi \tag{10}$$

where $\boldsymbol{F}$ is the subspace of load vectors, and ϕ is a vector of corresponding load magnitudes.

The resultant solution $\boldsymbol{u}$ of the Eq. (10) is an equilibrium surface that is parametrized using a vector of generalized displacements $\boldsymbol{\xi}$ and expanded up to the third order:

$$\boldsymbol{u} = \boldsymbol{u_\alpha}\xi_\alpha + \boldsymbol{u_{\alpha\beta}}\xi_\alpha\xi_\beta + \boldsymbol{u_{\alpha\beta\gamma}}\xi_\alpha\xi_\beta\xi_\gamma + O(||\boldsymbol{u}^4||) \quad \alpha,\beta,\gamma = 1,\ldots,m \tag{11}$$

where $\boldsymbol{u_\alpha}$, $\boldsymbol{u_{\alpha\beta}}$, and $\boldsymbol{u_{\alpha\beta\gamma}}$ represent the displacement fields and the mutual interactions between them; and m is the number of vectors selected in the force subspace while formulating the reduced-order model (ROM). The reduction subspace comprises the external force vector and additionally perturbation loads if unstable paths are of interest.

The equilibrium surface may be parametrized with an infinite choice of $\boldsymbol{\xi}$. Therefore, $\boldsymbol{\xi}$ is chosen such that it is a work conjugate to the load amplitudes so as to fix the parametrization:

$$(\boldsymbol{F}\phi)^t\delta\boldsymbol{u} = \phi^t\delta\boldsymbol{\xi} \tag{12}$$

Substituting Eq. (11) in the left-hand side of Eq. (12) and comparing coefficients of the $\delta\boldsymbol{\xi}$ terms, a set of orthogonality constraint equations is obtained as follows:

$$\begin{aligned} \boldsymbol{f}_\alpha^t\boldsymbol{u}_\beta &= \delta_{\alpha\beta}, \\ \boldsymbol{f}_\alpha^t\boldsymbol{u}_{\beta\gamma} &= 0, \\ \boldsymbol{f}_\alpha^t\boldsymbol{u}_{\beta\gamma\delta} &= 0 \end{aligned} \tag{13}$$

where $\boldsymbol{f}_\alpha$ is a component vector of the subspace $\boldsymbol{F}$, and $\delta_{\alpha\beta}$ is the Kronecker delta that is unity when $\alpha = \beta$.

The load amplitudes are similarly assumed to be a third-order expansion of the form

$$\phi = \bar{\boldsymbol{L}}(\boldsymbol{\xi}) + \bar{\boldsymbol{Q}}(\boldsymbol{\xi},\boldsymbol{\xi}) + \bar{\boldsymbol{C}}(\boldsymbol{\xi},\boldsymbol{\xi},\boldsymbol{\xi}) \tag{14}$$

where $\bar{\boldsymbol{L}}$, $\bar{\boldsymbol{Q}}$, and $\bar{\boldsymbol{C}}$ are representative of the stiffness tensors in a reduced-order system.

The load and displacement expansions in Eqs. (11) and (14) are then substituted into the equilibrium equation [Eq. (1)], and the coefficients of the various $\boldsymbol{\xi}$ terms are equated to zero. In combination with the orthogonality constraints, a system of equations is obtained that is then solved to obtain the unknown ROM variables. The following is the complete set of ROM equations:

$$\begin{bmatrix} \boldsymbol{L} & -\boldsymbol{F} \\ -\boldsymbol{F} & 0 \end{bmatrix} \begin{Bmatrix} \boldsymbol{u}_\alpha \\ \bar{\boldsymbol{L}}_\alpha \end{Bmatrix} = \begin{Bmatrix} \boldsymbol{0} \\ \boldsymbol{E}_\alpha \end{Bmatrix} \tag{15}$$

$$\begin{bmatrix} \boldsymbol{L} & -\boldsymbol{F} \\ -\boldsymbol{F} & 0 \end{bmatrix} \begin{Bmatrix} \boldsymbol{u}_{\alpha\beta} \\ \bar{\boldsymbol{Q}}_{\alpha\beta} \end{Bmatrix} = \begin{Bmatrix} -Q(\boldsymbol{u_\alpha},\boldsymbol{u_\beta}) \\ \boldsymbol{0} \end{Bmatrix} \tag{16}$$

Here, $\boldsymbol{E}_\alpha$ is a unit vector such that the α_{th} component of the vector is one and all other elements are zero. The equations show that together with the stiffness terms ($\bar{\boldsymbol{L}}_\alpha$, $\bar{\boldsymbol{Q}}_{\alpha\beta}$) of the ROM, the displacement fields $\boldsymbol{u}_\alpha$ and $\boldsymbol{u}_{\alpha\beta}$ are computed as byproducts. Unlike many eigenmode-based ROM approaches, there is no necessity for predefining appropriate coefficients in the displacement expansion. The computation of the term $\boldsymbol{Q}(\boldsymbol{u_\alpha},\boldsymbol{u_\beta})$ is done on an element level, and the global assembly is conducted thereafter, thus avoiding large tensor multiplications in the preprocessing steps. Furthermore, the cubic stiffness term is computed in a simplified form on the element level to avoid large tensor operations:

$$\begin{aligned} \bar{\boldsymbol{C}}_{\alpha\beta\gamma\delta} &= \boldsymbol{C}(\boldsymbol{u_\alpha},\boldsymbol{u_\beta},\boldsymbol{u_\gamma},\boldsymbol{u_\delta}) \\ &\quad -\frac{2}{3}[\boldsymbol{u}_{\alpha\beta}^t\boldsymbol{L}(\boldsymbol{u_{\delta\gamma}}) + \boldsymbol{u}_{\beta\gamma}^t\boldsymbol{L}(\boldsymbol{u_{\delta\alpha}}) + \boldsymbol{u}_{\gamma\alpha}^t\boldsymbol{L}(\boldsymbol{u_{\delta\beta}})] \end{aligned} \tag{17}$$

When no perturbation loads are included in the subspace, the ROM system is equivalent to a one-DOF polynomial equation, which can be easily solved using algebraic solvers without the need for iterative numerical procedures. This is only possible when there are no instabilities in the structural response.

C. Strategy for Nonlinear Analyses

1. *Preliminary Comparisons with Full Nonlinear FE Analysis*

Preliminary studies have been conducted on cantilevered and clamped–clamped beams. In these studies, a single step execution is conducted. This means that the ROM formulations are obtained only once in the initial undeformed state of the structure. In the case of the clamped–clamped beam, a concentrated force is applied at the midpoint along the beam length with a single step execution, and a load-deflection curve is obtained through the application of incremental loading. As shown in Fig. 1a, the results are found to be comparable between the ROM and the full FE analysis. The deviation in the response is 2.1%, even when a high degree of nonlinearity is reached at the maximum applied load of 1000 N. Contrary to these results, when a concentrated nonfollower force is applied at the tip of a cantilever beam, it is observed that a much larger than expected deflection response is obtained. A comparison of the results obtained from the ROM-based analysis with the results from a full FE analysis is shown in Fig. 1b. It can be observed that the ROM predictions, although nonlinear, are generally much higher than the reference. Furthermore, the error in response progressively increases as the applied load is increased from 0 to 70 N.

A closer investigation of the problem reveals that the large rotation of a cantilever is accompanied by a strongly coupled in-plane motion of the free end such that the out-of-plane and in-plane deflections are of a similar order of magnitude. This consequently results in considerable shifts in the location of the applied force in a global frame of reference and changes the internal force distribution across the structure due to the reduction in the moment arm. In comparison, for a clamped–clamped structure, a large deflection under an applied force results in a stretching effect that predominantly induces the nonlinearity. However, in this case, the in-plane deflections of the nodal points remain multiple orders of magnitude smaller than the out-of-plane deflections. This highlights the main difference between the large deflection behavior of a cantilever and a clamped–clamped structure. In addition to the large rotation effect, the changes in the geometry due to the structural deformations and the resultant changes in the states of the stresses and strains in the structure must be accounted for in the stiffness formulations. To resolve these issues, it is essential to reformulate the ROM-based governing equations at new equilibrium steps in the deformed state. In the next section, a

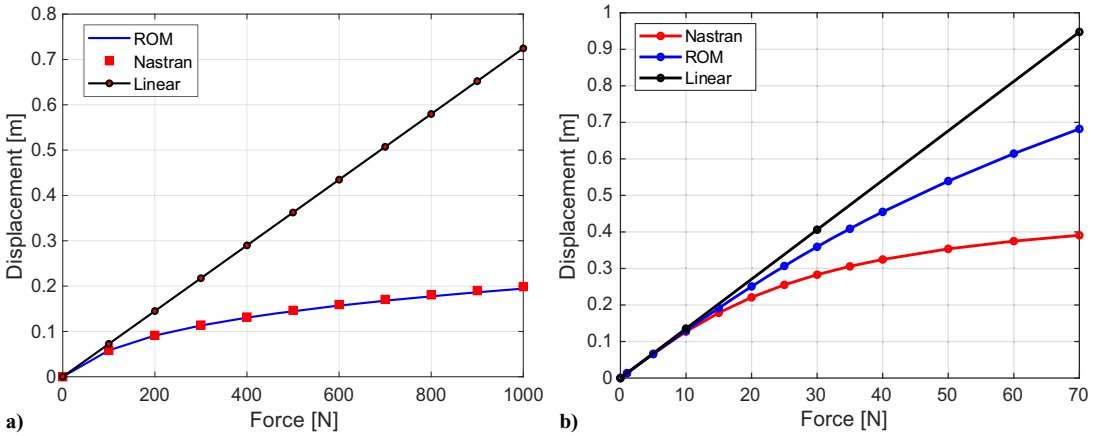

Fig. 1 Load-deflection response obtained using the ROM (with no stiffness update) compared to Nastran: a) for a clamped–clamped beam, and b) for a cantilever with an applied tip force.

stiffness updating procedure is described within the framework of the Koiter–Newton reduction method that can capture the influence of the large rotations in cantilevered structures.

2. *Process Schematic for Incremental ROM Updating*

A simplified process flow diagram for the nonlinear analysis framework is depicted in Fig. 2. The first step in the process is to obtain the full finite element model of the test structure. Here, the approach presented in Sec. II.A is followed. Then, a reduced subspace is selected to compute the ROM parameters. In the current implementation, a force subspace is used, comprising the external force vector. The ROM is then obtained through the process described in Sec. II.B. The incremental solution is obtained either using a Newton–Raphson solver or alternately using a polynomial solver if the ROM is a one-DOF system. A corrector step is then included to minimize the difference between the applied and internal forces. The concept of convective coordinates has been used in order to account for the large rotation of the structure. The nodal coordinates of the structure are updated after each load increment so that the local coordinate system of the element moves with the rigid-body motion of the structure and the equilibrium is computed in the deformed state. Finally, the stiffness tensors are updated in the current configuration of the structure, and a new load increment is provided to trace the equilibrium path.

The overall process can be broadly divided into 1) computation of the ROM variables, 2) solution of the ROM, and 3) correction of the displacements based on the internal forces. The computation of the ROM requires just one matrix inversion, i.e., the coefficient matrix described in Eqs. (14) and (15). The solution of the ROM is obtained using an algebraic polynomial solver for a stable 1-DOF system and adds a comparatively insignificant computation cost. Finally, there are N_k corrector steps in the k_{th} load increment, where each step requires one matrix inversion.

The number of matrix inversions $\mathcal{M}$ needed to solve the augmented finite element equations in n load increments is defined by

$$\mathcal{M} = \sum_{k=1}^{n} 1 + N_k \tag{18}$$

The primary advantage comes from the utilization of the nonlinear predictor, which allows larger load increments to be chosen. In comparison, most commercial FE tools use a linear predictor that necessitates the use of smaller load increments for faster convergence. The improvement in performance is highlighted in the Validation Results section (Sec. III).

III. Validation Results

To assess the effectiveness and accuracy of the process, verification studies were first conducted with respect to well-known benchmark problems available in the literature. Then, the process was validated through comparison with experimental results. The application to generic wing structures was demonstrated through the analysis of a high-aspect-ratio wing box. In the subsequent sections, the results of the validation study are presented. The following five test cases have been considered for the validation study: 1) beam rollup under tip moment, 2) cantilever plate subjected to tip shear force, 3) I-section cantilever with distributed loading and follower forces, 4) experimental results available for a flexible wing with tip load, and 5) a high-aspect-ratio wing box design similar in construction to a generic aircraft wing box.

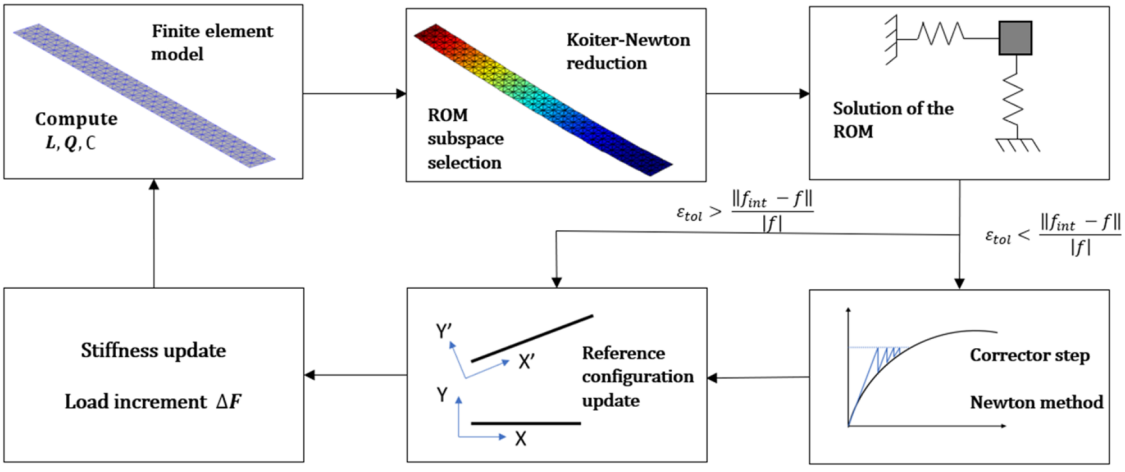

Fig. 2 Schematic of the iterative large deflection solver with incrementally updated ROM.

A. Comparison to Benchmark Problems

1. Cantilever Beam Rollup Under Applied Tip Moment

A classical benchmark problem for verification of nonlinear numerical methods is the beam rollup example where a tip loaded cantilevered structure under pure moment rolls up in a perfect circle. The dimensions of the structure are based on Ref. [33], in which all model parameters were defined as dimensionless. For consistency, the parameters are chosen to be in the International System of Units (SI) in the analyses conducted here. These model parameters are an elastic modulus of $E = 1.2e6$ or $1.2e+6$, a length of $L = 12$ m, a width of $b = 1$ m, a height of $h = 0.1$ m, and a Poisson's ratio of $\nu = 0$.

The applied maximum moment is $M = 50\pi/3$ N/m, which is increased from zero to the maximum using the user-defined and fixed incremental steps. The analysis is conducted using the beam element formulation in combination with the incrementally updated ROM method.

A comparison of the numerical results with the analytical solution is shown in Figs. 3a and 3b. A very good agreement is seen between the reference and the proposed method. The result presented in Fig. 3a has a deviation of 0.27% from the reference results at the maximum loading condition. The deviation is computed as the ratio of the norm of the vector comprising the error measure in the x and y directions to the norm of the tip deflection vector of the reference dataset. It is notable that an applied external moment implies that the sectional moment distribution across the structure does not vary over the load trajectory, unlike in the case of an applied force. Therefore, the influence of the large rotations on the internal load distribution is not a dominant factor in this example. Nevertheless, this analysis acts as a good validation case for the general nonlinear formulation, which is essential to capture the in-plane displacements correctly. Furthermore, it is noted that these results are achievable only when using the ROM update procedure, whereas it is impossible to capture the complete beam rollup with a single step execution with no ROM update. The simulation time for the analysis is 0.73 s, whereas the pre- and postprocessing require 2.8 s. The number of load increments used has an influence on the accuracy and efficiency of the analysis. The presented results are obtained using 50 load increments. By reducing the load increments to 30, it is possible to obtain the solution in 0.42 s with a deviation of 0.77% from the reference solution. Similarly, by increasing the load increments to 70, the simulation time increases to 0.95 s; however, the error reduces to 0.13%. All simulations here are conducted using a Windows computer with a 2.6 GHz processor and 16 GB of RAM.

2. Cantilever Flat Plate with an Applied Tip Shear Force

To further investigate the effectiveness of the proposed method, the large deflection behavior of a cantilevered plate subjected to a tip shear force is studied [33]. In this case, the analysis is conducted with flat shell elements to demonstrate the generality of the process, regardless of the FE formulation used, and it comprises 320 elements.

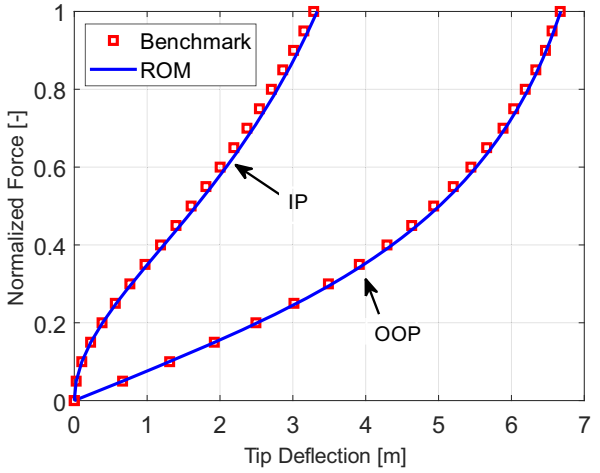

Fig. 4 Out-of-plane and in-plane displacements obtained using the ROM with applied normalized tip forces compared to the benchmark.

The dimensions of the structure are based on Ref. [33], in which all model parameters have been defined as dimensionless. For consistency, the parameters are chosen to be in SI in the analyses conducted here. These parameters are listed as follows: an elastic modulus of $E = 1.2e6$ or $1.2e+6$, a length of $L = 10$ m, a width of $b = 1$ m, a height of $h = 0.1$ m, and a Poisson's ratio of $\nu = 0$.

The applied maximum force is $P = 4EI/L^2$, which is increased from zero to the maximum using the user-defined and fixed 10 incremental steps.

A comparison between the results obtained using the incremental ROM-based method and the analytically obtained benchmark results is shown in Fig. 4. An error of 1.4% is seen in the tip deflection at maximum loading with a computational time of 2.1 s. By increasing the number of load increments to 20, this can be further reduced to under 0.8%; however, this is with almost twice the computational cost at 4.1 s. In this verification case, the problem setup is similar to the example of the cantilever discussed in Sec. II.C. However, as seen in the results, it is possible to capture the load-deflection response through the ROM updating procedure while obtaining a good agreement with the reference results.

3. Comparison Against the Modal Rotation Method

The MRM, briefly discussed in the Introduction section (Sec. I), has been shown to be effective for significantly large deflection problems with low computational times. Through this example, the performance of the ROM is compared against the MRM results. The structural model is an I-section cantilever beam for which the geometrical and material parameters are described in Ref. [21]. To summarize, the following parameters are used in the analysis: a length of $L = 30$ m, a total cross-section area of $A = 0.0152$ m^2,

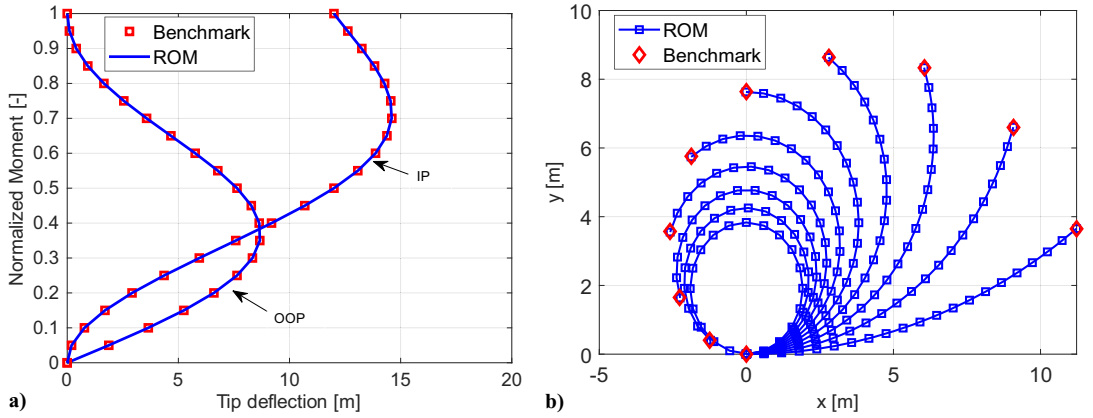

Fig. 3 Representations of a) out-of-plane (OOP) and in-plane (IP) displacements obtained using the ROM with an applied tip moment compared to Nastran, and b) incremental deflection of the cantilever at different load steps.

and an area moment of inertia of $I = 2.693\text{e}{-5}$ m^4. A uniformly distributed load of 1250 N/m is applied with the follower force effect enabled, which makes it closer to realistic wing loading conditions. The follower force effect implies that the applied force remains normal to the geometry in any deflected state.

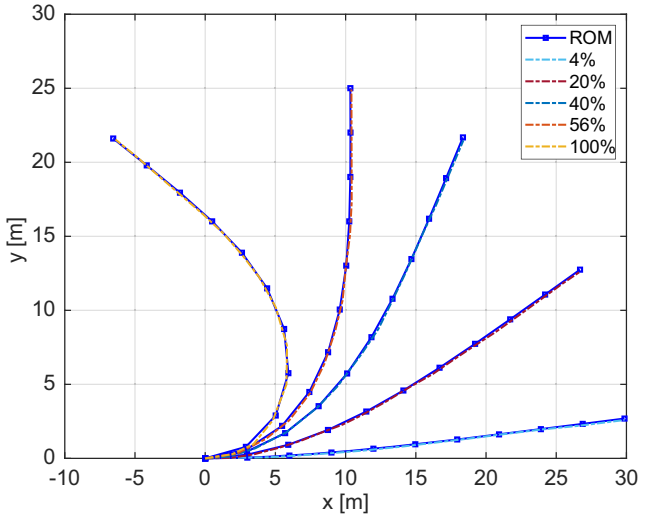

Fig. 5 Comparison of the deflection results for the distributed loading case against the MRM results at different fractions of the total load.

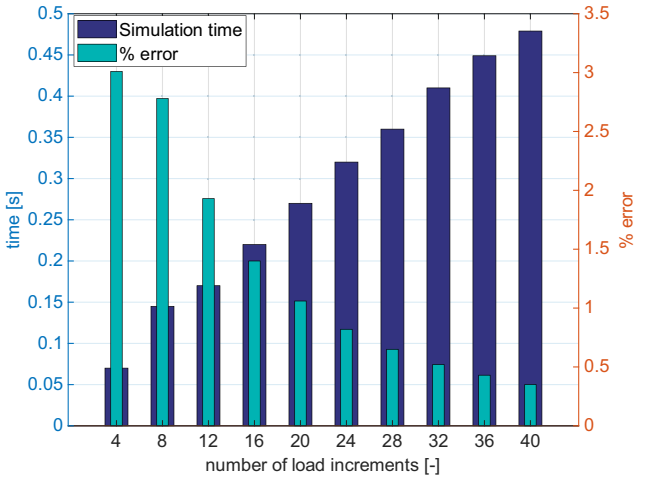

Fig 6 Depiction of the influence of the number of load intervals on the simulation time (in seconds) and accuracy of analysis (percent error) at a load of 700 N/m.

The results presented in Fig. 5 show a comparison of the computed beam deflections against the reference MRM results. The results show a good agreement with a maximum deviation of 0.83% at 100% loading. The maximum deflection presented here is computed using 40 load increments and requires a simulation time of 0.63 s with a total processing time of 2.1 s. Similar to test case 1, the accuracy varies with the number of load increments. The simulation time reduces to just 0.28 s if 18 load increments are used; however, the error increases to 2.4%. Furthermore, at lower loads, the results can be obtained much faster by using a lower number of load increments. For example, at 56% loading, the solution can be obtained with a 3.01% error in 0.07 s and four load increments. At 24 load increments, the simulation time increases to 0.32 s and the solution error reduces to 0.82%. The variations in the error and simulation time with the number of load increments are shown in Fig. 6. The simulation times are generally in a similar order of magnitude as the MRM. It is noteworthy that in this example, numerical convergence errors were seen in the Newton–Raphson iterations for loads beyond 1375 N/m, whereas the MRM could capture larger deflections.

B. Application to Wing Structures

1. *Experimental Validation: Pazy Wing*

The intended application of the proposed method is primarily to study the nonlinear structural behavior of highly flexible-wing structures. To demonstrate the applicability to realistic wing structures, the experimental data of static structural tests conducted on the Pazy wing were obtained. The Pazy wing is an aeroelastic benchmark wing specifically designed to study the geometrically nonlinear aeroelastic behavior of such wing structures through wind-tunnel tests and to generate benchmark experimental data for verification of numerical methods. The design, analysis, and testing of the Pazy wing were discussed in detail in Ref. [28,34]. The wing has been designed with a chord length of 100 mm and a span of 550 mm, and it can structurally sustain deformations up to 50–60% of the span. The primary structure is made of aluminum 7075, whereas a thin polyester foil is used to provide the aerodynamic shape of the wing. A tip mass attached at the center chord location is used to load and deform the structure during the pure bending tests. To conduct the analysis in the present study, an equivalent beam FE model [35,36] of the Pazy wing is used, as shown in Fig. 7b. The dimensions of the properties of the beam model are provided in Appendix C. The tip of the wing is loaded in steps using weights ranging from 0 to 3 kg.

A comparison of the out-of-plane tip deflection of the wing obtained using the ROM-based method, using experimental measurement data and through the full FE analysis using MSC Nastran, is shown in Fig. 8. Additionally, some results are obtained using the ROM-based model without updating the ROM incrementally, i.e., using single step executions. Overall, the results obtained using the proposed ROM-based method match well with the reference

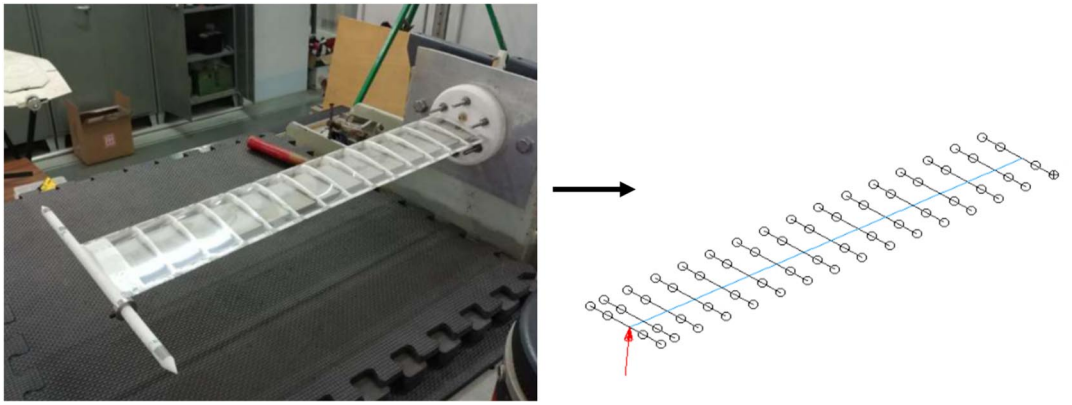

a) b)

Fig. 7 Representations of a) experimental setup and test structure of the Pazy wing developed in Ref. [28], and b) equivalent beam model of the Pazy wing depicted in blue along the spanwise direction with an applied tip load shown by the red arrow.

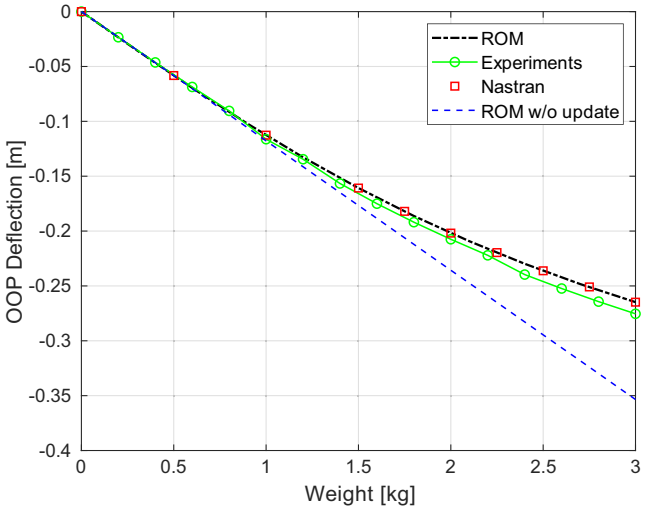

Fig. 8 Out-of-plane deflections of the Pazy wing obtained using the ROM with stiffness updates compared to MSC Nastran, experimental results, and ROM without stiffness update (w/o update).

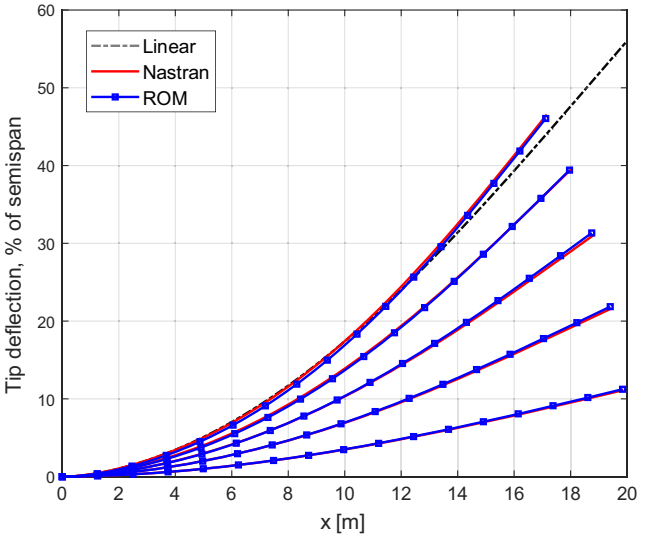

Fig. 10 Reference line deflection along the 40% chord position on the upper skin of the HAR wing box: comparison to MSC Nastran.

experimental results and with the full FE analysis when the incremental update procedure is used. A deviation of −2.5% is seen in comparison to the experiments, whereas the results match perfectly with Nastran. Both analyses are conducted with displacement and force convergence criteria with a tolerance of 1e-2, which is the default setting in Nastran. The full FE solution using Nastran required 985 iterative steps and a total time of 5 s to obtain the deflection at the maximum loading of 3 kg. The full solution curve shown in Fig. 8 is obtainable through the proposed method using 54 iterative steps and a total simulation time of 0.154 s for all load steps, with an additional 0.47 s needed for the pre- and postprocessing. The simulation for each load individually is even faster. For the maximum applied load of 3 kg, the solution can be obtained in 0.054 s with a processing time of 0.16 s. The reduction in iterative steps is aligned with the proposition in Sec. II.C that having a cubically nonlinear predictor step allows the possibility of larger load incremental steps, and therefore reduces the number of iterations needed. Furthermore, it is observed from Fig. 8 that when the ROM update is not conducted, the out-of-plane deflection almost follows a linear response path. This can be explained by the fact that the displacement dependent nonlinear stiffness terms are insignificant for this model when computed in the base undeformed state. This also ensures that the linear response is well matched within a linear domain of deflection.

2. *Verification Through FE Analysis: High-Aspect-Ratio Wing Box*

For the final test case, a wing box model with a 20 m half-span is considered. It is defined with anisotropic material properties and completely modeled using shell elements. The structural geometry is similar to the wing described in Ref. [20], albeit with the modification that the same material properties are defined at all sections of the geometry for simplicity. The elements of the material property matrix are defined as follows: $G_{11} = G_{22} = 79.15$ GPa, $G_{12} = 26.91$ GPa, and $G_{33} = 26.12$ GPa. The wing box comprises upper and lower skins, ribs, and spars: each with a varying thickness from the wingtip to the root. The variable thickness distribution is depicted in Fig. 9. The model is generated using the in-house parametric model generation tool, ModGen [37], from the DLR, German Aerospace Center and comprises 8660 triangular elements. The aerodynamic shape of the wing box has been defined using the NACA4412 and NACA4415 profiles.

The analysis is conducted with a distributed load acting along the 40% chord line, which consists of 160 unconstrained node points. At each of these node points, a transverse force of 500 N is applied, resulting in a total force of 80,000 N. Additionally, a 2000 N/m torsional moment is applied on each of the 160 node points to enforce a twisting motion in the structure. All degrees of freedom at the node points forming the profile at the root are fully constrained in the

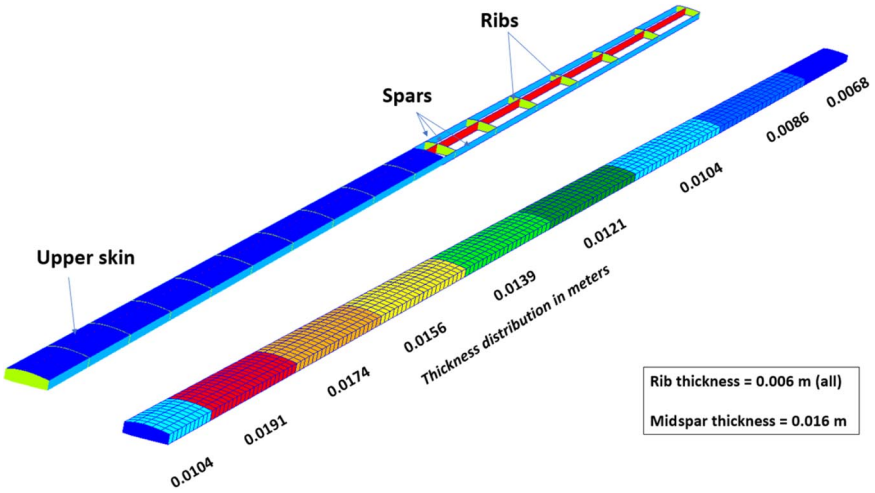

Fig. 9 Construction of the wing box and thickness distribution, in meters, along the wing half-span.

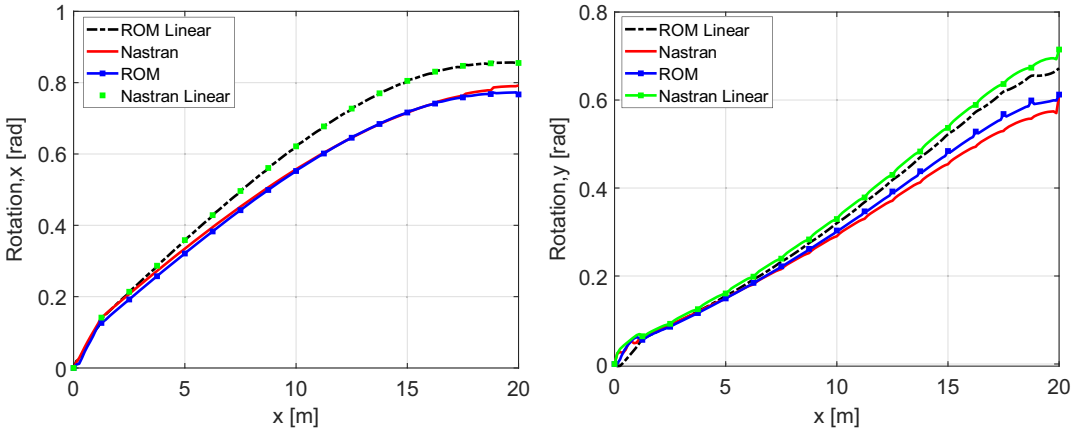

Fig. 11 Rotation due to transverse bending (left) and twist (right) along the length of the HAR wing box (40% chord line) compared to the results from Nastran.

analysis. Figure 10 shows the stepwise normalized deflection data along the reference line at the 40% chord position on the upper skin panel as a percentage of the semispan of the wing box. The peak transverse tip deflection is computed at 9.21 m, which is approximately 46% of the semispan. The error is computed as the ratio of the norm of the vector comprising the error measure in the x, y, and z directions to the norm of the reference tip deflection vector; and the solution is found to be deviating by 1.45% from the Nastran solution.

The rotation angles in transverse bending θ_1 and torsion θ_2 are also compared in this analysis, and the variation along the semispan is depicted in Fig. 11. The θ_1 is well matched with some distinctive deviations seen near the tip. The difference in the θ_2 estimation is slightly higher and is observed to be around 4.6% near the tip, whereas the error gradually becomes minimal toward the root. However, in contrast to θ_1, it is noticed that θ_2 in the linear analysis also deviates from the linear Nastran results, which implies the differences in the finite elements used have some influence on this result. The Nastran simulations require 395 iterations, whereas 11 iterations are sufficient to obtain the ROM results. Despite the reduction in the number of iterations, the total run time at 45.7 s is significantly higher for this model and overshoots the 42 s needed in Nastran. This increase is primarily due to the ROM formulation procedure; however, the high computational time is also partially attributed to suboptimal coding. It is inferred that with the increasing size and complexity of the model, the time needed for ROM formulation may have a contradictory effect on the efficiency of the model. Further investigations are needed to improve the efficiency of the algorithms used.

IV. Conclusions

A framework for the geometrically nonlinear analysis of structures undergoing large deflections is presented. The method incorporates a reduced-order modeling technique along with an incremental load application approach in order to trace the equilibrium path of the structure. The nonlinearity in the structure is introduced through the nonlinear strain-displacement relationship in combination with updating the coordinates of the structure to tackle the changing geometry and force location inherent to the deflection behavior of cantilevered structures. Validation studies have been conducted by comparing numerical results with common benchmark problems available in the literature. Data obtained from the static structural measurements conducted on the Pazy wing have been used for further verification of the numerical method. The framework is finally applied to a wing box model to demonstrate its applicability to generic structures, and the results are subsequently compared with MSC Nastran simulations.

Overall, the results are found to be sufficiently accurate in all the test cases. For large and complex models, the ROM formulation time can be significantly large. Further studies are required for improving the numerical efficiency of the ROM formulation algorithm for large models. A greater perceivable advantage of this ROM technique, however, is expected to be observed in dynamic analyses.

Appendix A: Beam Element

A.1. Strain and Curvature Definition of a Beam Element in Finite Element Framework

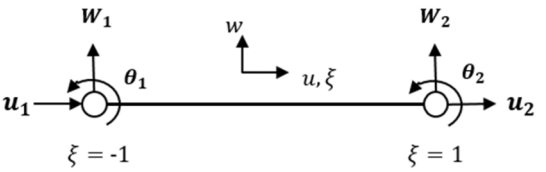

Fig. A1 Element degrees of freedom in the beam element.

The strain ε and the curvature χ for this element are defined as [32]

$$\varepsilon = \frac{(u_2-u_1)}{L} + \frac{1}{2}\left[\frac{(u_2-u_1)^2}{L} + \frac{6}{5L^2}(w_1-w_2)^2 + \frac{2}{15}(\theta_1-\theta_2)^2 + \frac{1}{5}\theta_1\theta_2 + \frac{1}{5L}(\theta_1+\theta_2)(w_1-w_2)\right]$$

$$\chi = -\frac{1}{L^2}\left[3w_1 - 3w_2 - \frac{6w_1x}{L} + \frac{6w_2x}{L} + (2L-3x)\theta_1 + (L-3x)\theta_2\right]$$

A.2. Linear Bending Stiffness Matrix for a Beam Element [32]

$$K_b = \begin{bmatrix} 0 & 0 & 0 & 0 & 0 & 0 \\ 0 & \frac{12EI}{L^3} & \frac{6EI}{L^2} & 0 & \frac{-12EI}{L^3} & \frac{6EI}{L^2} \\ 0 & \frac{6EI}{L^2} & \frac{4EI}{L} & 0 & \frac{-6EI}{L^2} & \frac{2EI}{L} \\ 0 & 0 & 0 & 0 & 0 & 0 \\ 0 & \frac{-12EI}{L^3} & \frac{-6EI}{L^2} & 0 & \frac{12EI}{L^3} & \frac{-6EI}{L^2} \\ 0 & \frac{6EI}{L^2} & \frac{2EI}{L} & 0 & \frac{-6EI}{L^2} & \frac{4EI}{L} \end{bmatrix}$$

Appendix B: Flat Shell Element

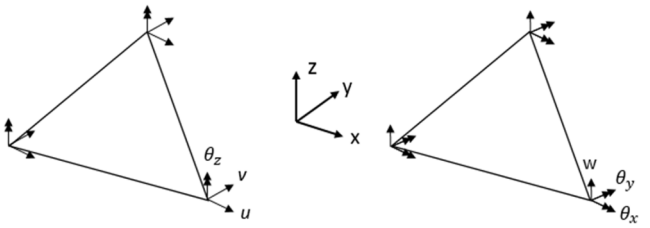

Fig. B1 Element degrees of freedom in the flat shell element.

The Strain in the Flat Shell Element is Defined as:

$$\varepsilon = \varepsilon_l + \varepsilon_{nl} = \left(\boldsymbol{B_l} + \frac{1}{2}\boldsymbol{B_{nl}}(\boldsymbol{q})\right)\boldsymbol{q}$$

$$\boldsymbol{B_l} = \frac{1}{2A}[\,\boldsymbol{B}_1 \quad \boldsymbol{B}_2 \quad \boldsymbol{B}_3\,]$$

where A is the element area.

Considering that the three nodal coordinates are $(x1, y1)$, $(x2, y2)$, and $(x3, y3)$,

$$x_{ij} = x_i - x_j$$
$$x_{ij} = x_i - x_j$$

$$\boldsymbol{B_1} = \begin{bmatrix} y_{23} & 0 & 0 & 0 & 0 & \dfrac{y_{23}(y_{13}-y_{21})}{6} \\ 0 & x_{23} & 0 & 0 & 0 & \dfrac{x_{32}(x_{32}-x_{12})}{6} \\ x_{32} & y_{32} & 0 & 0 & 0 & \dfrac{x_{31}y_{13}-x_{12}y_{21}}{3} \end{bmatrix}$$

$$\boldsymbol{B_2} = \begin{bmatrix} y_{31} & 0 & 0 & 0 & 0 & \dfrac{y_{31}(y_{21}-y_{32})}{6} \\ 0 & x_{13} & 0 & 0 & 0 & \dfrac{x_{13}(x_{12}-x_{23})}{6} \\ x_{13} & y_{31} & 0 & 0 & 0 & \dfrac{x_{12}y_{21}-x_{23}y_{32}}{3} \end{bmatrix}$$

$$\boldsymbol{B_2} = \begin{bmatrix} y_{12} & 0 & 0 & 0 & 0 & \dfrac{y_{12}(y_{32}-y_{13})}{6} \\ 0 & x_{21} & 0 & 0 & 0 & \dfrac{x_{21}(x_{23}-x_{31})}{6} \\ x_{21} & y_{12} & 0 & 0 & 0 & \dfrac{x_{23}y_{32}-x_{31}y_{13}}{3} \end{bmatrix}$$

The nonlinear strain component can be computed using the $\boldsymbol{B_{nl}}(\boldsymbol{q})$ term, which is given by

$$\boldsymbol{B}_{nl}(\boldsymbol{q}) = \begin{bmatrix} \boldsymbol{q}^t K_{xx} \\ \boldsymbol{q}^t K_{yy} \\ \boldsymbol{q}^t K_{xy} \end{bmatrix}$$

$$K_{xx} = \boldsymbol{B}_w^t \boldsymbol{T}_x^t \boldsymbol{T}_x \boldsymbol{B}_w + \boldsymbol{B}_v^t \boldsymbol{T}_x^t \boldsymbol{T}_x \boldsymbol{B}_v$$
$$K_{yy} = \boldsymbol{B}_w^t \boldsymbol{T}_y^t \boldsymbol{T}_y \boldsymbol{B}_w + \boldsymbol{B}_u^t \boldsymbol{T}_y^t \boldsymbol{T}_y \boldsymbol{B}_u$$
$$K_{xx} = \boldsymbol{B}_w^t (\boldsymbol{T}_x^t \boldsymbol{T}_y + \boldsymbol{T}_y^t \boldsymbol{T}_x) \boldsymbol{B}_w$$

Here,

$$\boldsymbol{T}_x = \frac{1}{2A}[\,y_{23} \;\; y_{31} \;\; y_{12}\,] \quad \text{and} \quad \boldsymbol{T}_y = \frac{1}{2A}[\,x_{32} \;\; y_{13} \;\; x_{21}\,]$$

The other terms involving $\boldsymbol{B}_u$, $\boldsymbol{B}_v$, and $\boldsymbol{B}_w$ are constant matrices consisting of zero and one. The explicit formulations of these matrices can be found in Refs. [26,32].

Appendix C: Dimensions of the Equivalent Beam Model of the Pazy Wing

The equivalent beam model is obtained through the University of Michigan's FEM2Stick framework [35,36]. The FE model consists of 16 node points located along the global x axis as follows:

$$X = [0.0; 0.03824; 0.07649; 0.11474; 0.15299; 0.19124; 0.22949; 0.26774; 0.30599; 0.34424; 0.38249; 0.42074; 0.45899; 0.49724; 0.53071; 0.54984]$$

The area of cross section of each element has minor variations and is defined as follows:

$$A = [9.7944e-6; 9.6666e-6; 9.6476e-6; 9.6487e-6; 9.6499e-6; 9.6506e-6; 9.6509e-6; 9.6509e-6; 9.6506e-6; 9.6499e-6; 9.6488e-6; 9.64716e-6; 9.6534e-6; 9.6992e-6; 1.0019e-7]$$

Similarly, the beam inertia has variations in each element and is defined as follows:

$$I = [5.2474; 4.5044; 4.4782; 4.4743; 4.4748; 4.4749; 4.4749; 4.4749; 4.4749; 4.4748; 4.4747; 4.4761; 4.4891; 4.5481; 4.7703]$$

Finally, an equivalent E modulus of 1.0 is used.

Acknowledgments

No specific funding has been received for this research. The authors would like to thank Markus Ritter of the DLR, German Aerospace Institute's Institute of Aeroelasticity, who is Head of the Large Deflection Working Group (LDWG). The authors would also like to thank the collaborating partner organizations of the LDWG for providing the experimental model and the experimental dataset used for verification purposes: respectively, University of Michigan, Ann Arbor, and Technion–Israel Institute of Technology.

References

[1] Bisshopp, K., and Drucker, D., "Large Deflection of Cantilever Beams," *Quarterly of Applied Mathematics*, Vol. 3, No. 3, 1945, pp. 272–275. https://doi.org/10.1090/qam/13360

[2] Noll, T. E., Brown, J. M., Perez-Davis, M. E., Ishmael, S. D., Tiffany, G. C., and Gaier, M., "Mishap Report," Investigation of the Helios Prototype Aircraft Mishap, NASA Tr 9, Vol. I, 2004.

[3] Patil, M., and Hodges, D., "On the Importance of Aerodynamic and Structural Geometrical Nonlinearities in Aeroelastic Behavior of High-Aspect-Ratio Wings," *Journal of Fluids and Structures*, Vol. 19, No. 7, 2004, pp. 905–915. https://doi.org/10.1016/j.jfluidstructs.2004.04.012

[4] Patil, M., Hodges, D., and Cesnik, C., "Nonlinear Aeroelastic Analysis of Complete Aircraft in Subsonic Flow," *Journal of Aircraft*, Vol. 37, No. 5, 2000, pp. 753–760. https://doi.org/10.2514/2.2685

[5] Patil, M., Hodges, D., and Cesnik, C., "Nonlinear Aeroelasticity and Flight Dynamics of High-Altitude Long-Endurance Aircraft," *Journal of Aircraft*, Vol. 38, No. 1, 2001, pp. 88–94. https://doi.org/10.2514/2.2738

[6] Patil, M., and Taylor, D., "Gust Response of Highly Flexible Aircraft," *47th AIAA/ASME/ASCE/AHS/ASC Structures, Structural Dynamics, and Materials Conference 14th AIAA/ASME/AHS Adaptive Structures Conference*, AIAA Paper 2006-1638, 2006.

[7] Cesnik, C., and Su, W., "Nonlinear Aeroelastic Modeling and Analysis of Fully Flexible Aircraft," *46th AIAA/ASME/ASCE/AHS/ASC*

Structures, Structural Dynamics and Materials Conference, AIAA Paper 2005-2169, 2005.

[8] Su, W., and Cesnik, C. E., "Dynamic Response of Highly Flexible Flying Wings," *AIAA Journal*, Vol. 49, No. 2, 2011, pp. 324–339. https://doi.org/10.2514/1.J050496

[9] Simpson, R., "Unsteady Aerodynamics, Reduced-Order Modelling, and Predictive Control in Linear and Nonlinear Aeroelasticity with Arbitrary Kinematics," Ph.D. Dissertation, Imperial College London, London, 2015.

[10] Hodges, D. H., "Geometrically Exact, Intrinsic Theory for Dynamics of Curved and Twisted Anisotropic Beams," *AIAA Journal*, Vol. 41, No. 6, 2003, pp. 1131–1137. https://doi.org/10.2514/2.2054

[11] Patil, M. J., and Hodges, D. H., "Flight Dynamics of Highly Flexible Flying Wings," *Journal of Aircraft*, Vol. 43, No. 6, 2006, pp. 1790–1799. https://doi.org/10.2514/1.17640

[12] Wang, L., "Nonlinear Aeroelastic Modelling of Large Wind Turbine Composite Blades," Ph.D. Dissertation, Univ. of Central Lancashire, Preston, England, U.K., 2015.

[13] Su, W., and Cesnik, C., "Strain-Based Geometrically Nonlinear Beam Formulation for Modeling Very Flexible Aircraft," *International Journal of Solids and Structures*, Vol. 48, Nos. 16–17, 2011, pp. 2349–2360. https://doi.org/10.1016/j.ijsolstr.2011.04.012

[14] Gai, G., Timme, S., and Badcock, K., "Reduced-Order Modelling of Nonlinear Aircraft Structures," *Royal Aeronautical Society—Applied Aerodynamic Conference*, July 2016.

[15] Muravyov, A. A., and Rizzi, S., "Determination of Nonlinear Stiffness with Application to Random Vibration of Geometrically Nonlinear Structures," *Computers and Structures*, Vol. 81, No. 15, 2003, pp. 1513–1523. https://doi.org/10.1016/S0045-7949(03)00145-7

[16] Wang, X. Q., Perez, R. A., and Mignolet, M. P., "Nonlinear Reduced Order Modeling of Complex Wing Models," *54th AIAA/ASME/ASCE/AHS/ASC Structures, Structural Dynamics, and Materials Conference*, AIAA Paper 2013-1520, 2013.

[17] Kim, K., Radu, A. G., Wang, X. Q., and Mignolet, M. P., "Nonlinear Reduced Order Modeling of Isotropic and Functionally Graded Plates," *International Journal of Non-Linear Mechanics*, Vol. 49, March 2013, pp. 100–110. https://doi.org/10.1016/j.ijnonlinmec.2012.07.008

[18] Ritter, M., Cesnik, C., and Krüger, W., "An Enhanced Modal Approach for Large Deformation Modeling of Wing-Like Structures," *56th AIAA/ASCE/AHS/ASC Structures, Structural Dynamics, and Materials Conference*, AIAA Paper 2015-0176, 2015.

[19] Ritter, M., and Cesnik, C., "Large Deformation Modeling of a Beam Type Structure and a 3D Wingbox Using an Enhanced Modal Approach," *57th AIAA/ASCE/AHS/ASC Structures, Structural Dynamics, and Materials Conference*, AIAA Paper 2016-1078, 2016.

[20] Ritter, M. R., "An Extended Modal Approach for Nonlinear Aeroelastic Simulations of Highly Flexible Aircraft Structures," Ph.D. Dissertation, Technical Univ. of Berlin, Berlin, Germany, 2019.

[21] Drachinsky, A., and Raveh, D. E., "Modal Rotations: A Modal-Based Method for Large Structural Deformations of Slender Bodies," *AIAA Journal*, Vol. 58, No. 7, 2020, pp. 3159–3173. https://doi.org/10.2514/1.J058899

[22] Cea, A., and Palacios, R., "A Non-Intrusive Geometrically Nonlinear Augmentation to Generic Linear Aeroelastic Models," *Journal of Fluids and Structures*, Vol. 101, Feb. 2021, Paper 103222. https://doi.org/10.1016/j.jfluidstructs.2021.103222

[23] Cea, A., and Palacios, R., "Geometrically Nonlinear Effects on the Aeroelastic Response of a Transport Aircraft Configuration," *Journal of Aircraft*, Vol. 60, No. 1, 2022, pp. 1–16. https://doi.org/10.2514/1.C036740

[24] Liang, K., Abdalla, M., and Gürdal, Z., "A Koiter-Newton Approach for Nonlinear Structural Analysis," *International Journal for Numerical Methods in Engineering*, Vol. 96, No. 12, 2013, pp. 763–786. https://doi.org/10.1002/nme.4581

[25] Liang, K., Ruess, M., and Abdalla, M., "The Koiter–Newton Approach Using von Kármán Kinematics for Buckling Analyses of Imperfection Sensitive Structures," *Computer Methods in Applied Mechanics and Engineering*, Vol. 279, Sept. 2014, pp. 440–468. https://doi.org/10.1016/j.cma.2014.07.008

[26] Sinha, K., Singh, N., Abdalla, M., De Breuker, R., and Alijani, F., "A Momentum Subspace Method for the Model-Order Reduction in Nonlinear Structural Dynamics: Theory and Experiments," *International Journal of Non-Linear Mechanics*, Vol. 119, March 2020, Paper 103314. https://doi.org/10.1016/j.ijnonlinmec.2019.103314

[27] Brauer, J., *What Every Engineer Should Know About Finite Element Analysis*, Marcel Dekker, New York, 1988, pp. 36–38.

[28] Avin, O., Drachinsky, A., Ben-Shmuel, Y., and Raveh, D. E., "Design of an Experimental Benchmark of a Highly Flexible Wing," *60th Israel Annual Conference on Aerospace Sciences (IACAS)*, 2020, pp. 1–18.

[29] Tiso, P., "Finite Element-Based Reduction Methods for Static and Dynamic Analysis of Thin-Walled Structures," Ph.D. Dissertation, Delft Univ. of Technology, Delft, The Netherlands, 2006.

[30] Militello, C., and Felippa, C. A., "The First ANDES Elements: 9-DOF Plate Bending Triangles," *Computer Methods in Applied Mechanics and Engineering*, Vol. 93, No. 2, 1991, pp. 217–246. https://doi.org/10.1016/0045-7825(91)90152-V

[31] Alvin, K., de la Fuente, H., Haugen, B., and Felippa, C., "Membrane Triangles with Corner Drilling Freedoms—I. The EFF Element," *Finite Elements in Analysis and Design*, Vol. 12, Nos. 3–4, 1992, pp. 163–187. https://doi.org/10.1016/0168-874X(92)90033-9

[32] Liang, K., "A Koiter–Newton Arclength Method for Buckling-Sensitive Structures," Ph.D. Dissertation, Delft Univ. of Technology, Delft, The Netherlands, 2013.

[33] Sze, K. Y., Liu, X. H., and Lo, S. H., "Popular Benchmark Problems for Geometric Nonlinear Analysis of Shells," *Finite Elements in Analysis and Design*, Vol. 40, No. 11, 2004, pp. 1551–1569. https://doi.org/10.1016/j.finel.2003.11.001

[34] Avin, O., Raveh, D. E., Drachinsky, A., Ben-Shmuel, Y., and Tur, M., "An Experimental Benchmark of a Very Flexible Wing," *AIAA SciTech 2021 Forum*, AIAA Paper 2021-1709, 2021.

[35] Riso, C., Sanghi, D., Cesnik, C. E. S., Vetrano, F., and Teufel, P., "Parametric Roll Maneuverability Analysis of a High-Aspect-Ratio-Wing Civil Transport Aircraft," *AIAA SciTech Forum*, AIAA Paper 2020-1191, 2020, pp. 1–23.

[36] Riso, C., and Cesnik, C. E., "Low-Order Geometrically Nonlinear Aeroelastic Modeling and Analysis of the Pazy Wing Experiment," *AIAA SciTech 2022 Forum*, AIAA Paper 2022-2313, 2022.

[37] Klimmek, T., "Parametric Set-Up of a Structural Model for FERMAT Configuration for Aeroelastic and Loads Analysis," *Journal of Aeroelasticity and Structural Dynamics*, Vol. 3, No. 2, 2014, pp. 31–49.

R. Ohayon
Associate Editor